nature communications

Article

https://doi.org/10.1038/s41467-025-60284-5

High-performance Ag_2Se-based thermoelectrics for wearable electronics

Received: 28 January 2025

Accepted: 20 May 2025

Published online: 29 May 2025

Check for updates

Lin Zhang[1,2,5], Xiao-Lei Shi[3,5], Hongjing Shang[1,2,4] ✉, Hongwei Gu[1,2,4], Wenyi Chen[3], Meng Li[3], Daxing Huang[1,2,4], Hao Dong[1,2], Xiaolei Wang[1,2], Fazhu Ding[1,2,4] ✉ & Zhi-Gang Chen[3] ✉

Flexible thermoelectric materials and devices hold enormous potential for wearable electronics but are hindered by inadequate material properties and inefficient assembly techniques, leading to suboptimal performance. Herein, we developed a flexible thermoelectric film, comprising Ag_2Se nanowires as the primary material, a nylon membrane as a flexible scaffold, and reduced graphene oxide as a conductive network, achieving a record-high room-temperature ZT of 1.28. Hot-pressed Ag_2Se nanowires exhibited strong (013) orientation, enhancing carrier mobility and electrical conductivity. Dispersed reduced graphene oxide further boosts electrical conductivity and induces an energy-filtering effect, decoupling electrical conductivity and the Seebeck coefficient to achieve an impressive power factor of 37 μW cm^{-1} K^{-2} at 300 K. The high-intensity between Ag_2Se and reduced graphene oxide interfaces enhance phonon scattering, effectively reducing thermal conductivity to below 0.9 W m^{-1} K^{-1} and enabling the high ZT value. The nylon membrane endowed the film with exceptional flexibility. A large-scale out-of-plane device with 100 pairs of thermoelectric legs, assembled from these films, delivers an ultrahigh normalized power density of >9.8 μW cm^{-2} K^{-2}, outperforming all reported Ag_2Se-based flexible devices. When applied to the human body, the device generated sufficient power to operate a thermo-hygrometer and a wristwatch, demonstrating its practical potential for wearable electronics.

The growing adoption of self-powered wearable electronics has accelerated advancements in portable energy harvesting technologies[1]. Among these, thermoelectric generators (TEGs), which enable direct conversion between heat and electricity, have gained significant attention for their battery-free operation and low maintenance costs[2]. Flexible wearable TEGs with high output performance are particularly advantageous, as their adaptability to various curvatures ensures optimal thermal contact and efficient energy conversion[3]. Integrating flexible substrates with flexible thermoelectric films provides distinct benefits over rigid thermoelectric legs, which often require reduced thickness to achieve flexibility. This trade-off diminishes temperature differences (ΔT) and lowers power density (ω)[4]. However, due to the limited thickness of thermoelectric films, traditional film-based TEGs are typically designed with an in-plane structure, where the film aligns parallel to the substrate[5]. This configuration reduces the contact area with heat sources and limits ΔT, restricting such devices to functioning as signal sources for sensors rather than as power supplies for wearable

[1]Key Laboratory of Applied Superconductivity and Institute of Electrical Engineering, Chinese Academy of Sciences, Beijing, China. [2]University of Chinese Academy of Sciences, Beijing, China. [3]School of Chemistry and Physics, ARC Research Hub in Zero-emission Power Generation for Carbon Neutrality, and Centre for Materials Science, Queensland University of Technology, Brisbane, QLD, Australia. [4]Institute of Electrical Engineering and Advanced Electromagnetic Drive Technology, Qilu Zhongke, and Shandong Key Laboratory of Advanced Electromagnetic Conversion Technology, Jinan, China. [5]These authors contributed equally: Lin Zhang, Xiao-Lei Shi. ✉e-mail: shanghongjing@mail.iee.ac.cn; dingfazhu@mail.iee.ac.cn; zhigang.chen@qut.edu.au

electronics[6–8]. To overcome these limitations, rational device design is crucial. Optimized designs should maximize the collection of body heat across large areas while efficiently utilizing cross-plane ΔT, thereby enhancing the practical applicability of film-based TEGs in powering wearable electronic devices.

In addition to optimizing TEG structures[9], the development of high-performance thermoelectric materials is a crucial strategy for advancing efficient flexible thermoelectric devices[10]. The thermoelectric performance of materials is quantified using the dimensionless figure of merit, $ZT = S^2\sigma T/\kappa$[11,12], where S, σ, $S^2\sigma$, T, and κ represent the Seebeck coefficient, electrical conductivity, power factor, absolute temperature, and thermal conductivity, respectively. Among thermoelectric thin-film materials, Bi_2Te_3-based films are renowned for their exceptional thermoelectric performance[13]. However, their high cost[14] and inherently layered structure[15] limits their flexibility and adaptability for wearable applications. Moreover, achieving high-performance flexible Bi_2Te_3 films often relies on expensive equipment and complex fabrication processes, such as magnetron sputtering to deposit materials onto flexible substrates[16]. These challenges significantly hinder their scalability and broader application of Bi_2Te_3 films. Therefore, exploring cost-effective and flexible alternatives is imperative for advancing the practicality of thermoelectric devices in wearable technologies.

Ag_2Se has recently attracted significant attention for thermoelectric properties, with ZT values comparable to those of Bi_2Te_3 near room temperature[17], making it highly promising for converting low-grade thermal energy into electricity. To enhance the thermoelectric performance and flexibility of Ag_2Se thin films[18–24], various strategies and methods have been developed to enhance the thermoelectric performance and flexibility, including adjusting the synthesis temperature[25], tuning the ratio of Ag/Se[26,27], hybridizing with polymers[28–31], sandwich engineering[32], and doping with other elements (e.g., Cu[33] and S[34]). Notably, inducing a strong (013) orientation in polycrystalline Ag_2Se films has been shown to improve carrier mobility (μ) and σ[19,35–39], as demonstrated in studies utilizing techniques like Te doping for orientation optimization[40]. Beyond doping and conventional compositional optimization, reducing grain-boundary resistance in thin films has emerged as an effective strategy for improving σ. Grain-boundary resistance significantly hinders μ at lower temperatures (below 500 K), which negatively impacts σ[41,42]. Increasing grain size to reduce grain boundary intensity has shown promise in addressing this issue. However, much of the current research overly prioritizes achieving a high $S^2\sigma$ while overlooking κ and the overall ZT. Notably, high σ, often responsible for elevated $S^2\sigma$ values, can adversely affect ZT [43], by increasing both electronic (κ_e) and lattice thermal conductivity (κ_l), as $\kappa = \kappa_l + \kappa_e$. Larger grain sizes, which reduce phonon scattering at grain boundaries, may further increase κ_l, complicating efforts to optimize overall thermoelectric performance. Achieving a high ZT while maintaining an elevated $S^2\sigma$ remains a critical and ongoing challenge for Ag_2Se-based thermoelectric thin films.

Results and discussion

To address these challenges, we propose an innovative structural design for a high-performance, highly flexible thermoelectric film. This film incorporates Ag_2Se nanowires as the primary components, reduced graphene oxide (rGO) as a conductive network, and a nylon membrane as a flexible supporting scaffold, resulting in a film with exceptional thermoelectric performance and remarkable flexibility. Through the hot-pressing process, Ag_2Se nanowires with protrusions form a film with a strong (013) orientation, which enhances the intrinsic μ and σ. The incorporation of rGO forms a conductive network, which further improves the electron mobility in the film, boosting the film's σ (Fig. 1a and Supplementary Fig. 1). The uniform dispersion of rGO forms high-intensity Ag_2Se-rGO interfaces, which enhance the scattering of phonons, while activating the energy filtering effect[44], effectively decoupling the σ and the S. As a result, this synergy achieves an impressive $S^2\sigma$ of 37 μW cm^{-1} K^{-2} at 300 K, with a high S of −158 μV K^{-1} and σ of 1481 S cm^{-1}, significantly outperforming previous reports (Fig. 1b)[22,27,30,34,40,45–53]. Moreover, high-intensity Ag_2Se-rGO interfaces effectively suppress κ_l (~0.09 W m^{-1} K^{-1}), reducing κ below 0.9 W m^{-1} K^{-1} and enabling a high ZT value of 1.28. The nylon membrane, serving as a flexible scaffold, endows the film with outstanding mechanical flexibility. In contrast, the solvothermal method offers a more economical alternative to vacuum coating technologies, such as magnetron sputtering and pulsed laser deposition, which typically require costly equipment and high-purity targets. Further, compared to Bi_2Te_3, Ag_2Se demonstrates superior thermoelectric performance, greater flexibility, and lower material costs (Fig. 1c). Inspired by arched bridge structures, we fabricated a large-area (14 × 14 cm^2) out-of-plane TEG, as shown in Fig. 1d. This TEG, composed of 100 pairs of thermoelectric legs based on the Ag_2Se-rGO film, achieved a highly competitive ω of 6.7 mW cm^{-2} obtained at ΔT of 26 K (Fig. 1e), as well as an outstanding normalized power density (ω_n) exceeding 9.8 μW cm^{-2} K^{-2}. This ω_n value is higher than that of most published TEGs based on thin films[5] and even TEGs based on bulk materials[54]. When applied to the human body, the wearable TEG generated sufficient electrical energy to power a thermo-hygrometer and a wristwatch, demonstrating its immense potential for practical applications in wearable electronics, particularly in human health monitoring.

Microstructure analysis

To investigate the influence of varying rGO content on the thermoelectric performance of Ag_2Se films, we defined the samples as $Ag_2Se + x$ wt% rGO films, where x = 0, 0.01, 0.02, 0.03, and 0.04. Unlike previous reports, this work employed a high-temperature-assisted ultrasonication method, instead of conventional aging techniques to promote the growth of Ag_2Se nanowires. The novelty of this approach lies in a three-step synthesis process: first, well-dispersed Se nanowires are prepared using high-temperature-assisted ultrasonication; second, during the synthesis of highly reactive Ag_2Se nanowires at elevated temperatures, rGO is uniformly incorporated; and finally, dense composite films with highly crystallized grains fabricated by employing an optimized hot-pressing process. The synthesis mechanism is detailed in Supplementary Fig. 2. In the initial stage, amorphous α-Se particles are formed (Supplementary Fig. 3a), which subsequently develop into crystalline t-Se seeds that gradually grow into Se nanowires. High-temperature-assisted ultrasonication plays a crucial role in coordinating the uniform formation of nuclei and promoting the growth of Se particles. Comparative studies with nanowires fabricated using low-temperature ultrasonication or non-ultrasonicated aging methods confirm this mechanism. In these cases, many unconverted Se particles and small Se nanowires were observed (Supplementary Fig. 3b, c). This is because the combination of high temperature and ultrasonication enhances the surface activity of α-Se, accelerating t-Se nucleation and growth rates, thereby forming nanowires with superior crystallinity[55,56]. This method not only eliminates the time-consuming aging process, significantly improving preparation efficiency, but also produces Se nanowires with better crystallinity, higher uniformity, and excellent dispersion (100–120 nm in diameter), as demonstrated in Supplementary Fig. 4[28,34,45]. In contrast, extending the ultrasonication time (e.g., up to 3 min) results in shorter and irregularly shaped nanowires, likely due to the rapid formation of excessive t-Se seeds during the brief ultrasonication process (Supplementary Fig. 3d).

Using these Se nanowires as templates, we synthesized Ag_2Se nanowires at higher temperatures than those reported in previous studies[25,26,28,29,45]. The elevated temperatures accelerated the bonding between Ag and Se, further promoting the formation of Ag_2Se nanowires with superior crystallinity (Fig. 2a and Supplementary Fig. 5). Interestingly, certain protrusions formed on the Ag_2Se nanowires,

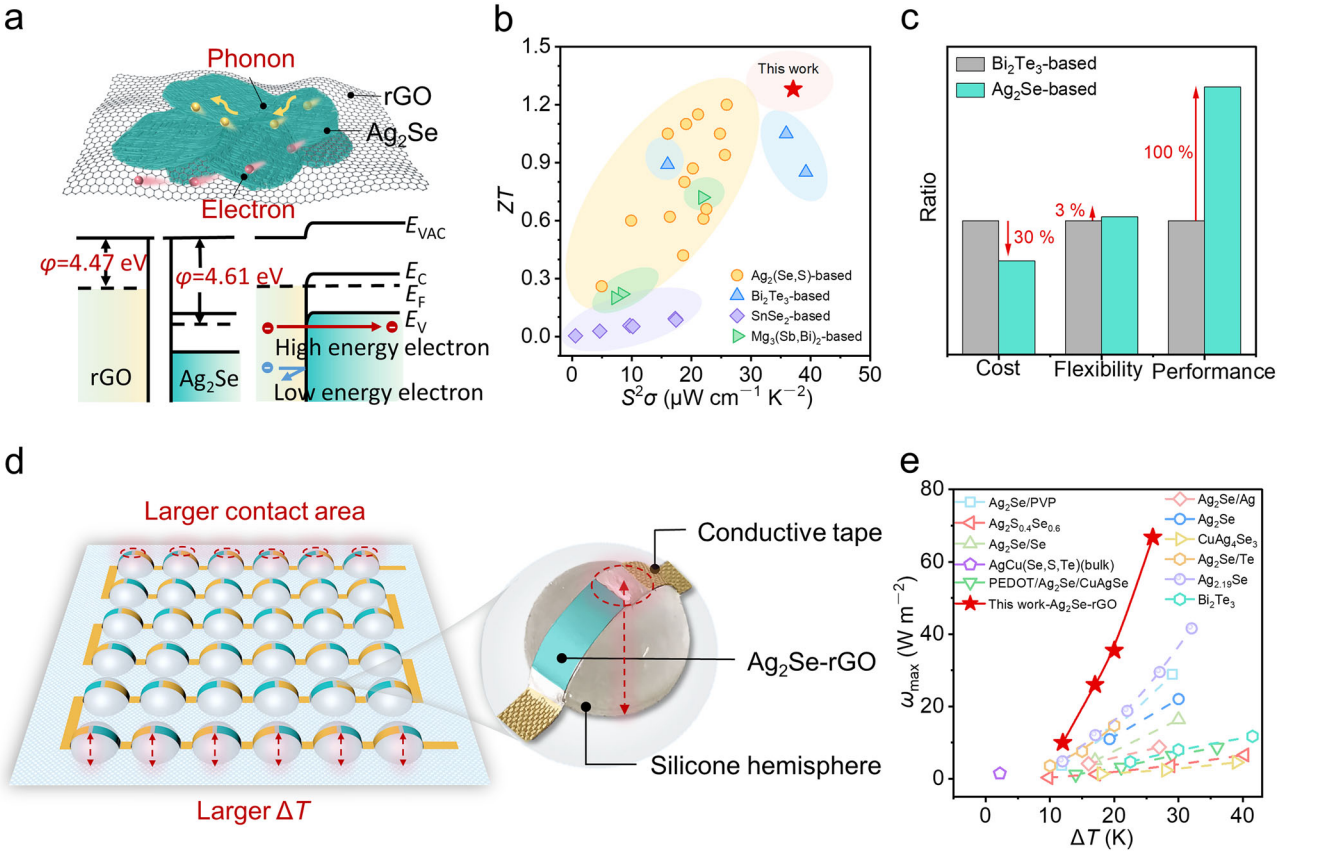

Fig. 1 | Introduction of high-performance Ag_2Se films and out-plane thermoelectric generator (TEG) for wearable electronics. a Transport mechanism of phonons and electrons within Ag_2Se-rGO films. Here rGO is abbreviated from reduced graphene oxide. **b** Room-temperature *ZT* between this work and some representative reports[22,27,30,34,40,45–53,75–78]. **c** Comparison of materials cost, flexibility, and performance between Ag_2Se and Bi_2Te_3 fabricated by solvothermal methods[3]. **d** Image of the TEG in this work. **e** Comparison of power density (ω) values between this work and reported Ag_2Se- and Bi_2Te_3-based TEGs[4,19,25–28,30,33,34,40,79].

which can be attributed to the higher surface energy and activity at the edges and tips of the nanowires[57–60]. These protrusions offer significant benefits during the hot-pressing process by increasing the contact area between nanowires, improving adhesion, and enhancing the mechanical strength of the resulting films (Supplementary Fig. 6). Additionally, the irregular protrusions exhibit higher reactivity, allowing them to interact more readily with neighboring nanowires. This interaction promotes stable assemblies and facilitates grain crystallization and growth, leading to films with superior structural properties. As a result, the prepared films exhibited better crystallization, reduced porosity, and higher density compared to previous reports[25,26,29,33,45,52] (Fig. 2b, c and Supplementary Figs. 7 and 8). Furthermore, the (013) pole figure analysis revealed high-intensity red and yellow regions, indicating a strong preferential (013) orientation in the Ag_2Se films. This alignment suggests that the nanowires' growth direction optimizes carrier transport by favoring a high σ, which is crucial for enhancing thermoelectric performance. After incorporating rGO into the material matrix, the Ag_2Se grain sizes became even larger (Fig. 2e, f and Supplementary Figs. 9 and 10). This is because in addition to the high intrinsic mobility, rGO can also act as active nucleation sites, promoting the nucleation and growth of Ag_2Se grains during the hot-pressing process[61,62]. Additionally, rGO increases the specific surface area of the material, improving grain contact and interaction, which further encourages the formation of larger grain[63]. Remarkably, despite the larger grain sizes, the films retained their highly (013)-orientated feature, maintaining their favorable carrier transport properties. At the macroscopic level, the films exhibit a silver-white metallic luster, indicative of their high quality and dense structure. This dense structure enhances light reflection while reducing transmission and absorption, as shown in Supplementary Fig. 11, further validating the excellent densification and overall quality of the films[46].

To explore the micro/nanostructure and composition of Ag_2Se-rGO film, high magnification SEM (Supplementary Fig. 12) and transmission electron microscopy (TEM) (Supplementary Fig. 13) were used for detailed characterization. There are no obvious pores in the Ag_2Se-rGO films. Furthermore, a typical cross-sectional TEM image reveals that amorphous material is surrounded by crystalline regions of Ag_2Se (Fig. 2g). Energy-dispersive spectroscopy (EDS) elemental mapping confirmed the crystalline regions as Ag_2Se and the amorphous regions as rGO. Importantly, the Ag_2Se grains showed excellent integration with the rGO, ensuring a well-connected structure conducive to enhanced thermoelectric performance. High-resolution TEM (HRTEM) images focused on Ag_2Se grains adjacent to rGO (Fig. 2h and Supplementary Fig. 13), particularly in three regions highlighted by yellow, red, and blue squares in Fig. 2h and Supplementary Fig. 13b. These regions displayed clear lattice fringes, indicating excellent crystallinity. Interestingly, all three regions had nearly identical lattice spacings of ~0.38 nm, consistent with the (002) plane of Ag_2Se. This uniformity suggests that the regions either belong to a single large grain or represent coherent grain boundaries, which are highly advantageous for charge transport by minimizing electron scattering. The corresponding selected area electron diffraction (SAED) patterns and fast Fourier transform images for the three regions (Fig. 2h and Supplementary Figs. 13e and 13f) revealed identical patterns, confirming their alignment along the Ag_2Se [210] zone axis. Such structural coherence further underscores the high crystallinity and order within the composite material. Additionally, the rGO layer within the composite was found to have a thickness of approximately ~29 nm (Fig. 2i). The

https://doi.org/10.1038/s41467-025-60284-5

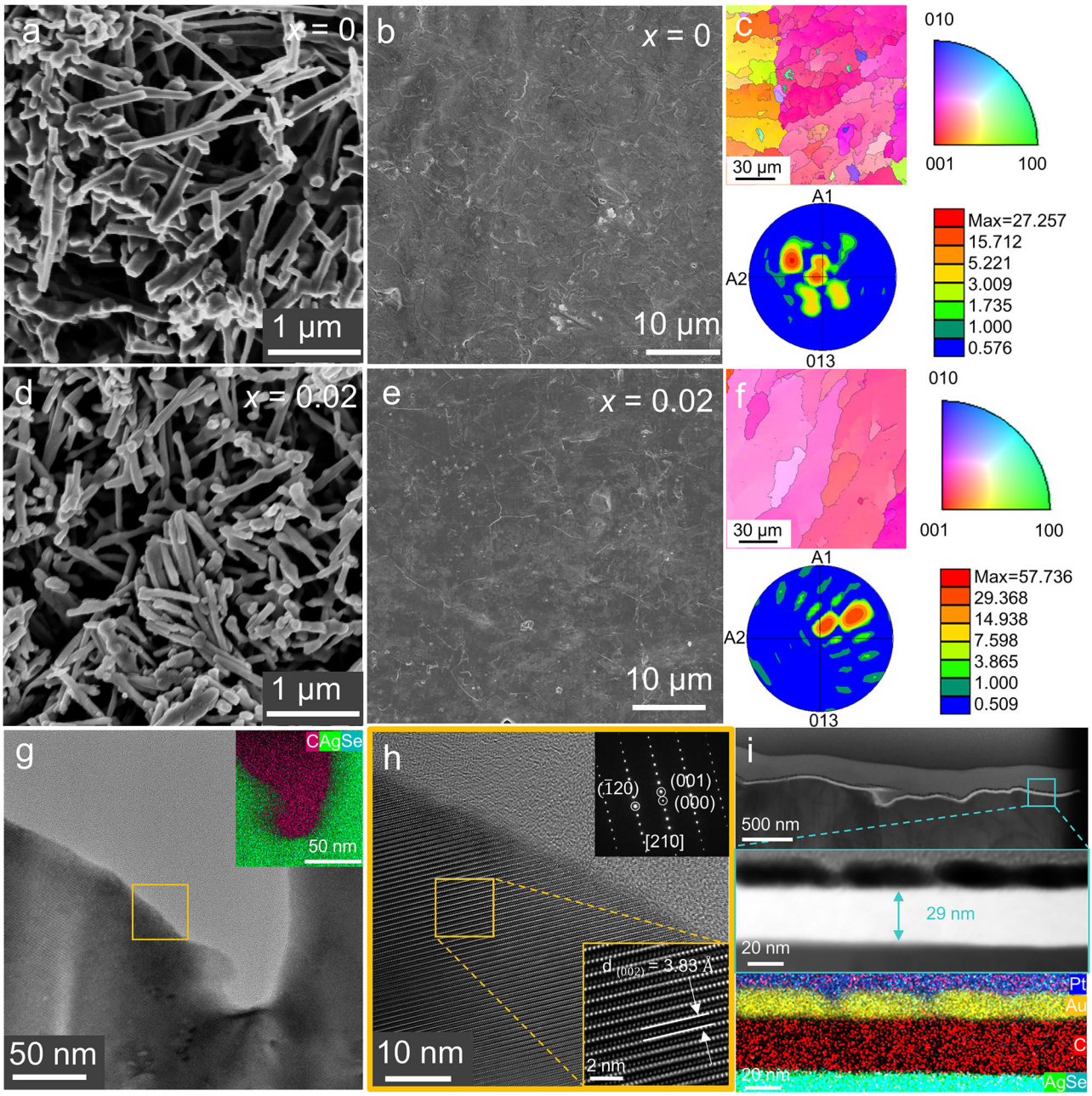

Fig. 2 | Morphological characterization of the $Ag_2Se + x$ wt% rGO films. **a**, **b** Scanning electron microscopy (SEM) images of Ag_2Se nanowires and Ag_2Se film, (**c**) Electron backscattered diffraction (EBSD) image and polar diagram along the (013) direction of Ag_2Se film. **d**, **e** SEM images of Ag_2Se + 0.02 wt% rGO nanowires and Ag_2Se film, **f** EBSD images and pole files along the (013) direction of Ag_2Se film. **g** Transmission electron microscopy (TEM) image (the inset is the energy-dispersive spectroscopy (EDS) mapping of different elements). **h** High-resolution TEM (HRTEM) images of the marked yellow square in (**g**) (the inset is the corresponding enlarged image and SAED pattern). **i** rGO distributed in Ag_2Se film and the corresponding EDS mapping.

thinness of the rGO is attributed to its low concentration in the matrix and the improved dispersion facilitated by hydrogen bonding between ethylene glycol and the oxygen-containing functional groups on rGO. This optimized dispersion ensures that the rGO is uniformly distributed, further supporting its effectiveness in enhancing the thermoelectric properties of the composite[64].

To evaluate the crystallinity of Se nanowires and Ag_2Se films synthesized at different temperatures, X-ray diffraction (XRD) patterns were analyzed (Supplementary Figs. 14 and 15). The Se nanowires exhibited excellent crystallinity, with all diffraction peaks corresponding to Se (JCPDS #06-0362). For the Ag_2Se films, all peaks corresponded to Ag_2Se (JCPDS #24-1041), confirming the successful synthesis of the material. Interestingly, as the synthesis temperature increased from 60 °C to 100 °C, the diffraction peaks shifted from (112) and (121) to (013), indicating that optimizing the synthesis temperature is essential for achieving desired orientation of Ag_2Se crystals. After incorporating rGO into the films, a strong (013) orientation was observed, which is beneficial for achieving high μ (Supplementary Fig. 16a)[24], aligning with the results from electron backscattered diffraction (EBSD) (Fig. 2f)[25]. Furthermore, density-functional theory (DFT) calculations indicate that the (013) orientation sets the ground for high mobility and good electronic transport. Since characteristic peaks of rGO are difficult to observe in XRD, Raman spectroscopy was employed to analyze the Ag_2Se-rGO composite films (Supplementary

Fig. 16b). Two prominent peaks were observed at approximately 1344 and 1583 cm^{-1}, corresponding to the D-band and G-band of rGO[65], confirming the successful incorporation of rGO into the Ag_2Se matrix.

Further composition and bonding analysis were conducted using X-ray photoelectron spectroscopy (XPS) (Supplementary Figs. 16c–f and Supplementary Figs. 17, 18, and 19). For GO, the C 1s peak was deconvoluted into three components located at 284.78, 286.78, and 288.48 eV, corresponding to C-C, C-O, and O-C=O bonds, respectively (Supplementary Fig. 16d)[66]. In the Ag_2Se-rGO composite films, the C 1s spectrum was reduced to two peaks: one at 284.78 eV (C-C) and the other at 286.78 eV (C-O), with the intensity of the C-O peak significantly diminished. This confirms that graphene oxide (GO) was successfully reduced to rGO.

The XPS spectra of Ag_2Se + 0.02 wt% rGO were similar to those of pristine Ag_2Se, with peaks corresponding to Ag 3$d_{3/2}$, Ag 3$d_{5/2}$, Se 3$d_{3/2}$, and Se 3$d_{5/2}$, respectively (Supplementary Fig. 16c). However, the binding energies of Ag 3d and Se 3d in Ag_2Se-rGO composites showed upward shift compared to pure Ag_2Se (Supplementary Fig. 16e, f), indicating stronger bonding interactions within the composite[67]. These binding energy shifts were also observed in samples with different rGO concentrations (x = 0.01, 0.03, and 0.04 wt%) (Supplementary Figs. 17, 18, and 19). The stronger interfacial interactions between Ag_2Se nanowires and rGO, driven by the high surface energy of rGO, enhance the bonding between the nanowires. This facilitates the formation of more stable large grains during the hot-pressing process, ultimately contributing to the enhanced performance of the composite films[63,68].

Thermoelectric properties of Ag_2Se-based films

The thermoelectric performance of Ag_2Se films prepared at different synthesis temperatures is presented in Supplementary Fig. 20. All films exhibit negative S, confirming their n-type conductivity. Notably, while the S shows minimal variation across the samples, the σ increases initially and then decreases as the synthesis temperature rises. The Ag_2Se film synthesized at 90 °C demonstrates the highest σ, reaching approximately 1342 S cm^{-1} at ~300 K. As a result, this film achieves a significantly higher $S^2\sigma$ compared to previously reported Ag_2Se-based thermoelectric materials (Supplementary Table 2).

To enhance the thermoelectric performance of Ag_2Se films, varying concentrations of rGO were incorporated into the film matrix. The addition of rGO increased the absolute S ($|S|$) compared to pure Ag_2Se films (Fig. 3a), primarily by reducing carrier concentration (n, Fig. 3b). Due to the energy filtering effect, low-energy carriers are selectively scattered at the interfaces, leading to a reduction in the number of effective carriers within the composites. However, the μ and energy of the remaining charge carriers are enhanced, ultimately resulting in the synergistic optimization of both σ and S. The σ initially increased before declining with higher rGO concentration. Notably, the Ag_2Se + 0.02 wt% rGO film exhibited the highest σ among all samples in the 300–400 K range, reaching ~1481 S cm^{-1} at 300 K (Fig. 3c), comparable to that of Ag_2Se single crystals[53]. This optimized combination of S and σ, enables the Ag_2Se + 0.02 wt% rGO film achieving a room-temperature $S^2\sigma$ of ~37 μW cm^{-1} K^{-2} (Fig. 3d), representing the highest value reported for Ag_2Se-based thermoelectric materials to date (Fig. 3e and Supplementary Table 2). Moreover, an average $S^2\sigma$ ($S^2\sigma_{avg}$) between 300 and 390 K reached an impressive 41 μW cm^{-1} K^{-2}, signifying a major advancement in Ag_2Se-based thermoelectric research (Supplementary Fig. 21). Additional testing on three samples produced consistent results (Supplementary Fig. 22).

To understand the origins of the high $S^2\sigma$, we analyzed the μ (Fig. 3f and Supplementary Fig. 23). As the doping concentration of rGO increases, the μ of the films first increases and then decreases. Notably, the Ag_2Se + 0.02 wt% rGO film exhibits an exceptional μ of approximately 1500 $cm^2V^{-1}s^{-1}$ at room temperature, ranking among the highest values reported to date. Even the pristine Ag_2Se film achieves a high μ of around 1100 $cm^2V^{-1}s^{-1}$, consistent with previously reported values. The high μ observed in these films can be attributed to two key factors: (1) the pronounced (013) orientation in the Ag_2Se films, which significantly enhances carrier transport; and (2) the incorporation of rGO, which possesses high intrinsic μ and forms a continuous conductive network with Ag_2Se nanowires[69], This network not only improves inter-nanowire bonding but also facilitates efficient carrier transfer. As a result, all Ag_2Se + x wt% rGO films exhibit higher μ compared to the undoped Ag_2Se counterpart. However, excessive rGO addition (e.g., 0.04 wt%) leads to aggregation and increased carrier scattering, thereby reducing both μ and σ. We further calculated the density-of-states effective mass (m^*), using the single parabolic band (SPB) model (Fig. 3g). Despite the reduction in n with increasing rGO content, m^* remained high. This indicates that the intensive interfaces between rGO and Ag_2Se induce an energy filtering effect, decoupling the S and the σ to enhance both parameters simultaneously. Additionally, the deformation potential energy (E_{def}) of the films was calculated. The results showed that the E_{def} decreased with increasing rGO content (Fig. 3g). A lower E_{def} reflects greater lattice deformability, suggesting improved plasticity. This enhanced plasticity not only maintains structural stability but also improves flexibility during bending, making the composite films highly suitable for flexible thermoelectric applications. Furthermore, the electrical properties of the films were enhanced after the incorporation of an appropriate amount of single-walled carbon nanotubes (SWCNTs) into the Ag_2Se composite (Supplementary Fig. 24). We believe that these experimental findings may provide valuable insights for enhancing the thermoelectric performance of Ag_2Se-based composites in future studies.

To access the thermoelectric performance, we measured the in-plane κ of the films, which was approximately 0.87 W m^{-1} K^{-1} at 300 K (Fig. 3h and Supplementary Table 3). Although the film exhibited a relatively high κ_e, the κ_l was successfully suppressed to 0.09 W m^{-1} K^{-1} due to the high-intensity Ag_2Se-rGO interfaces. As a result, the ZT value reached ~1.28 at 300 K, marking the highest performance reported for Ag_2Se-based films to date (Fig. 1b). This value is comparable to that of state-of-the-art Bi_2Te_3 films and bulk Ag_2Se materials[22,25–30,34,40,45–53,70,71], highlighting the exceptional thermoelectric performance of the fabricated films. It should be noted that due to inherent limitations in thermal conductivity measurement techniques of film, the parallel model was used to evaluate the thermal conductivity (the related details were provided in Supplementary Information), where the interfacial thermal resistance between Ag_2Se-rGO film and substrate was ignored, which may limit the accuracy of thermal conductivity measurement. Therefore, the ZT value is for reference only.

To evaluate the practicality of the films, we assessed their stability and flexibility (Fig. 3i and Supplementary Fig. 25). The electrical properties were evaluated over 10 consecutive thermal cycles, with each comprising heating from 300 to 380 K and subsequent cooling back to 300 K. The results revealed negligible changes in σ, S, or $S^2\sigma$, confirming excellent thermal stability. Mechanical flexibility was analyzed by measuring the normalized conductivity (Fig. 3i) (σ/σ_0, where σ_0 and σ represent the initial and measured conductivity values) as a function of bending cycles. Flexibility improved with increasing rGO content, aligning with the E_{def} trends (Fig. 3g). Notably, the Ag_2Se + 0.02 wt% rGO film retained 96.9% of its initial σ after 1500 bending cycles at a bending radius (r) of 5 mm. Under a bending radius of 4 mm, the σ loss of the Ag_2Se + 0.02 wt% rGO film after 500 bending cycles was less than 4% (Supplementary Fig. 26), demonstrating exceptional flexibility, durability, and suitability for flexible thermoelectric applications (Supplementary Table 2). The main reasons for the enhancement of mechanical flexibility properties by rGO are as follows: First, the unique two-dimensional structure of rGO imparts exceptionally high Young's modulus and tensile strength, which significantly reinforces the mechanical performance of the Ag_2Se-based composite[72]. Second, a small amount of rGO can be uniformly

https://doi.org/10.1038/s41467-025-60284-5

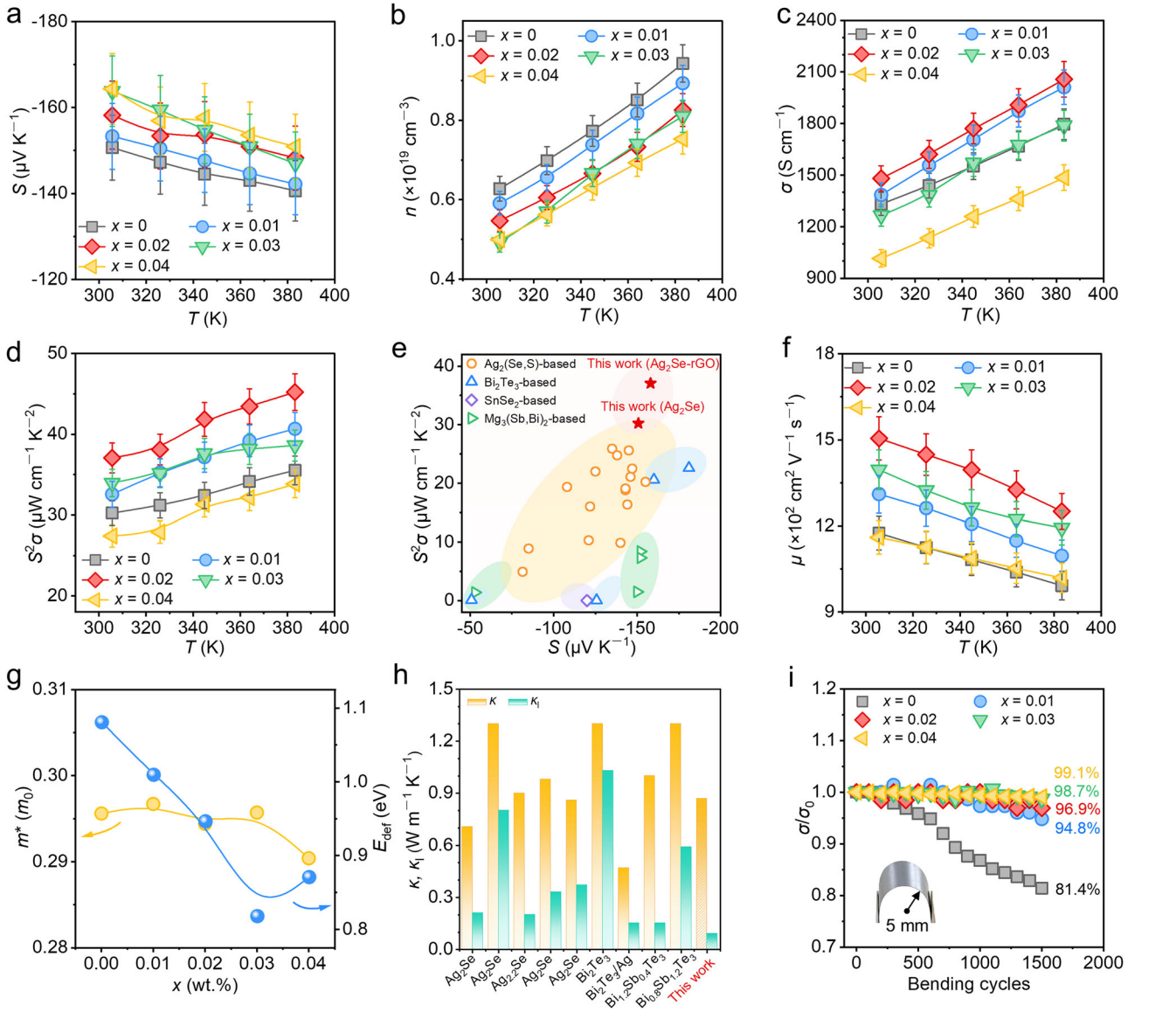

Fig. 3 | Thermoelectric properties, stability, and flexibility of $Ag_2Se + x$ wt% rGO films. Temperature-dependent (**a**) Seebeck coefficient (S), (**b**) Hall carrier concentration (n), (**c**) electrical conductivity (σ), and (**d**) $S^2\sigma$. **e** Comparison of $S^2\sigma$ for reported films and this work[6,22,25,26,28–30,34,40,45–49,51–53,75,79–84]. **f** Temperature-dependent mobility (μ). **g** x-dependent effective mass (m^*) and deformation potential (E_{def}). **h** Room-temperature thermal conductivities (κ) and lattice conductivities (κ_l) between this work and some representative reports[19,25,53,78,79,85]. **i** Change in σ (σ/σ_0) dependent on bending cycles for $Ag_2Se + x$ wt% rGO films (bending radius $r = 5$ mm).

dispersed within and intimately contact the Ag_2Se matrix, forming a continuous conductive network that facilitates optimized stress distribution and improves the overall load-bearing capacity[73]. Finally, the strong interfacial bonding between rGO and the Ag_2Se matrix enhances stress transfer efficiency, thereby further improving the material's strength and flexibility[74].

High-performance thermoelectric generator

A soft, comfortable, and breathable fabric substrate was selected for the wearable TEG. A silicone hemisphere was incorporated to create leveraging its specific hardness and compressibility for multiple functions: supporting the thermoelectric legs, enhancing the contact area with the heat source, and establishing a significant temperature gradient. The smooth curvature of the hemisphere ensured strong adhesion to the thermoelectric legs, effectively preventing breakage or damage caused by limited flexibility, thereby improving device stability. Flexible conductive tape was used to connect the thermoelectric legs, allowing the TEG to bend during wear, while indium solder at the joints ensured reliable electrical contact (Supplementary Fig. 27).

A TEG comprising 100 pairs of thermoelectric legs was fabricated, with dimensions of ~14 × 14 cm^2. The TEG design is highly adaptable and can be customized into various shapes and sizes as required (Supplementary Fig. 28). The open-circuit voltage (V_{oc}) of the TEG increased linearly with the ΔT (Fig. 4a), reaching a maximum of ~408 mV at $\Delta T = 26$ K. Figure 4b, c illustrates the relationship between the device voltage (V), output power (P), load current (I) at different ΔTs. The V decreased proportionally with the I. At $\Delta T = 12$ K, the maximum power (P_{max}) was ~15 μW, corresponding to an internal resistance (R_{in}) of the TEG (~453 Ω). At $\Delta T = 26$ K, the P_{max} reached approximately 100 μW with the R_{in} reducing slightly to ~449 Ω. Under these conditions, the TEG achieved a highly competitive ω of 6.7 mW cm^{-2} and an excellent ω_n of over 9.8 μW cm^{-2} K^{-2}, demonstrating tremendous potential for practical applications (Supplementary Table 4).

https://doi.org/10.1038/s41467-025-60284-5

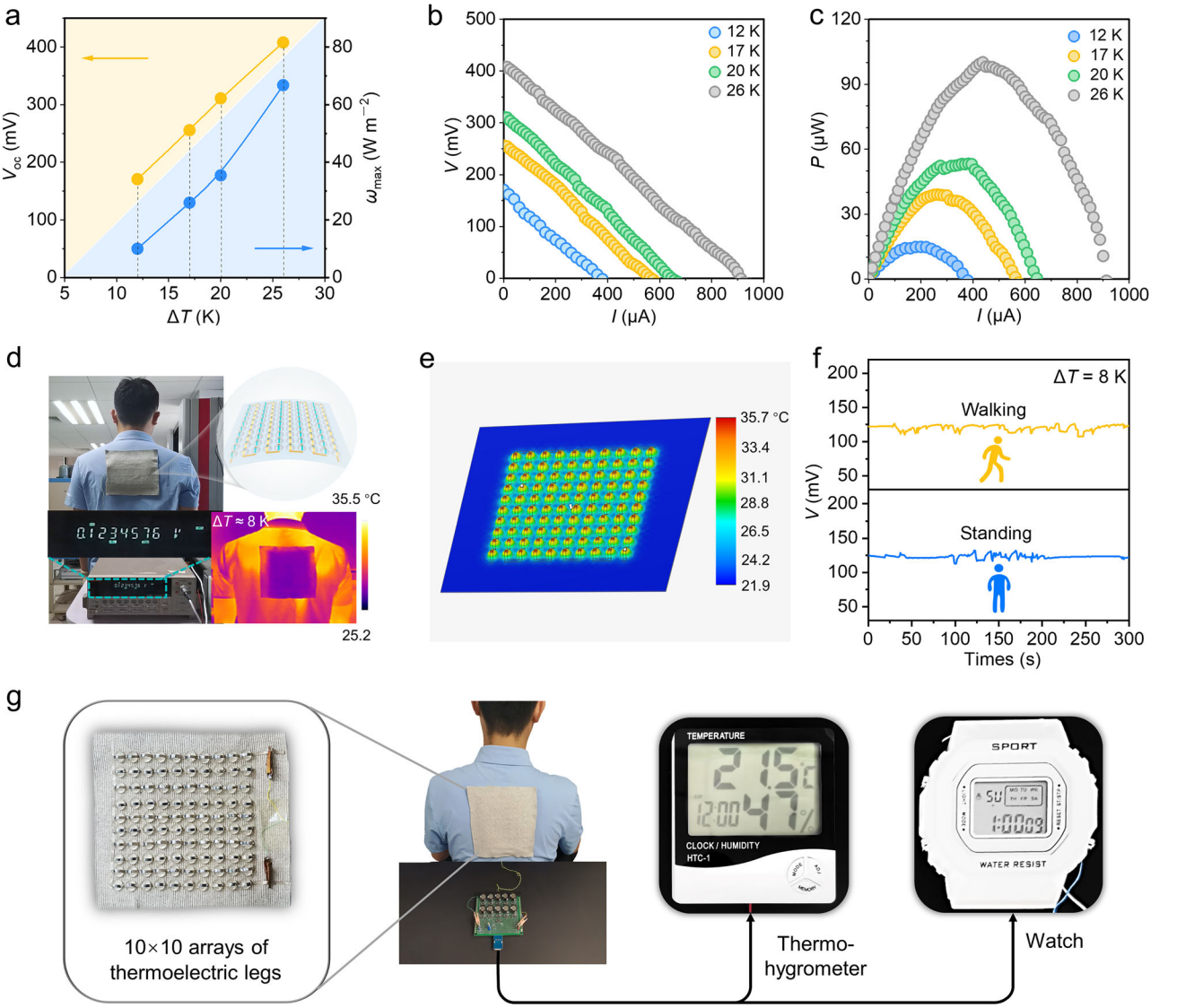

Fig. 4 | Device performance. a Open-circuit voltages (V_{oc}) and ω of out-plane TEG with 100-Ag_2Se + 0.02 wt% rGO legs evaluated at various temperature differences (ΔTs). **b** Voltage (V) and (**c**) output power (P) as a function of current (I) at various ΔTs. **d** Optical images of generating voltage based on the ΔT between the human body and environment (the inset is the corresponding front view of TEG and infrared thermal image). **e** Temperature distribution of the simulated TEG. **f** Continuous monitoring of the V of the human wearing the TEG at different states. **g** Diagram of charging supercapacitors by using the human body and powering a thermo-hygrometer and watch.

To evaluate the output performance of the TEG in practical applications, the device was evaluated while worn on the back of a human subject (Fig. 4d). At an ambient temperature of 25 °C, the TEG achieved an out-of-plane ΔT of ~8 K, as confirmed by infrared imaging. This ΔT corresponded to a V_{oc} of ~123 mV, closely aligning with the simulated results (Fig. 4e). To monitor the continuous output performance of the TEG, the subject alternated between standing still and walking for 300 s while wearing the device (Fig. 4f). The results demonstrated that stable operation throughout the test, maintaining a V of ~120 mV, underscoring the TEG's reliability and promising potential for practical wearable applications.

To explore the potential of utilizing the energy generated from the ΔT between the human body and the environment, the TEG was used to charge ten parallel capacitors to approximately 70 mV. These capacitors were then reconfigured in series, producing a V of ~0.7 V. This output was subsequently amplified using a boost converter, as depicted in the circuit diagram (Fig. 4g and Supplementary Fig. 29). The generated energy successfully powered a thermo-hygrometer (1.5 V) and a wristwatch (3 V), demonstrating that the out-of-plane TEG, with a carefully optimized design, can continuously and stably supply sufficient energy for low-power electronic devices. Looking forward, the development of larger-area TEGs to exploit greater temperature gradients could significantly increase energy output, enabling the power supply for higher-power devices such as smartphones. This underscores the promising applications of TEG technology in wearable electronics and sustainable energy solutions.

In summary, we fabricated Ag_2Se/rGO/nylon films with exceptional thermoelectric performance. The films, consisting of Ag_2Se nanowires, exhibit a macroscopic (013) orientation after hot pressing, which enhances the μ and σ. The well-dispersed rGO further boosts the σ and the S through the energy filtering effect, while the intensive interfaces effectively reduce the κ. As a result, the films achieve a record-high $S^2\sigma$ of 37 μW cm^{-1} K^{-2} and a ZT value of 1.28 at 300 K, establishing a new benchmark for Ag_2Se-based materials. Additionally, an advanced out-of-plane TEG with 100 pairs of thermoelectric legs, incorporating silicone hemispheres, was constructed using these films,

leveraging a giant temperature difference between the human body and the environment to directly power a thermo-hygrometer and a wristwatch. These findings indicate the tremendous potential of Ag_2Se-based materials for practical applications in wearable electronics and health monitoring, paving the way for future energy-harvesting technologies.

Methods

Materials

L-Ascorbic acid, selenium dioxide, and $AgNO_3$ were purchased from Sinopharm Chemical Reagent Co., Ltd. (China). GO was supplied by The Sixth Element (Changzhou) Materials Technology Co., Ltd. *β*-Cyclodextrin was obtained from Shanghai Aladdin Biochemical Technology Co., Ltd. Ethylene glycol (EG, >99%) was sourced from Alfa Aesar.

Preparation of Se nanowires

1 g SeO_2 and 1 g *β*-cyclodextrin were added to 100 mL distilled water and stirred until fully dissolved, forming solution A. Separately, 1 g *L*-ascorbic acid was added to 100 mL distilled water and stirred until completely dissolved, forming solution B. Solution A was then slowly added dropwise into solution B under continuous stirring, resulting in the mixed product. After stirring for 4 h, the product was extracted, filtered, and centrifuged with absolute ethanol at least three times. Notably, before each centrifugation, the mixture was ultrasonically shaken in a warm water bath (~45 °C) for ~90 s. Finally, the brown Se nanowires were collected by filtration.

Preparation of Ag_2Se-rGO nanosheets

To prevent the agglomeration of graphene in solution, GO was selected as the precursor to synthesize rGO by a reduction reaction in an EG solution. First, a specified amount of $AgNO_3$ was dissolved in an appropriate volume of EG to form solution C. Next, a predetermined quantity of the as-prepared Se nanowires (n_{Ag}:n_{Se} = 2:1) and GO were added to solution C, and the mixture was stirred at 90 °C for 2 hours to ensure a sufficient reaction. After cooling to room temperature, ethanol was added to precipitate the $Ag_2Se + x$ wt% rGO nanosheets. This process was repeated three times to remove any residual reactants.

Preparation of Ag_2Se-rGO composite films

$Ag_2Se + x$ wt% rGO composite films were fabricated through vacuum filtration using a nylon membrane. The resulting films were dried at 80 °C for 5 min and then hot-pressed at 200 °C for 30 min under a pressure of 1 MPa. Based on the weight percentages of rGO in the composite films (0.01, 0.02, 0.03, and 0.04 wt.%), the samples were designated as $x = 0$, $x = 0.01$, $x = 0.02$, $x = 0.03$, and $x = 0.04$, respectively.

Assembly of the flexible thermoelectric generator

Silicone hemispheres with a diameter of 5 mm, arranged in a 10 × 10 array, were fixed onto a flexible and breathable fabric at regular intervals. The film of Ag_2Se + 0.02 wt% rGO was selected as thermoelectric legs due to its excellent performance. Thermoelectric legs with dimensions of 8 × 2.5 mm^2 were attached to the silicone hemispheres, with both ends of the legs coated with silver paste. Once the silver colloid solidified, the other half of the hemispheres was covered with flexible conductive tape to connect the thermoelectric legs. To further minimize contact resistance and improve the stability of the device, indium solder was used to weld the Ag_2Se-rGO legs to the conductive tapes, ensuring the reliable electrical connection. The temperature applied at the top of the hemisphere was taken as the high-temperature end, while the temperature of the fabric was taken as the low-temperature end, taking the difference between the two as the ΔT.

Characterization

Morphology analysis was performed using scanning electron microscopy (SEM, ZEISS SIGMA, FEI-Siron), EBSD (EDAX OIM 6.0), and TEM (Thermo Scientific Talos F200S G2 200 kV). The TEM samples were prepared using a focused ion beam (FIB, Thermo Scientific Scios 2 DualBeam). Structural analysis was conducted using XRD (Bruker D8 four-circle diffractometer), Raman spectroscopy (Renishaw inVia, with an excitation wavelength of 532 nm), XPS (Thermo Scientific K-Alpha), and ultraviolet photoelectron spectroscopy (UPS, Thermo Fisher Scientific ESCALAB XI+). The temperature-dependent S and σ were measured simultaneously using commercial equipment (ZEM-3, ULVAC Riko, Japan) in a helium atmosphere (within ±5% uncertainty). The S and σ of all specimens were measured using bilayer films deposited on a nylon substrate, with a specimen size of 5 × 15 mm^2. As the nylon substrate is non-conductive, the measured thickness corresponds solely to that of the thermoelectric films (Ag_2Se-rGO). n and μ were determined using a Van der Pauw Hall measurement system (NYMS), with a measurement uncertainty of ~5%. Flexibility was measured by fixing one end of the film, while the other end was bent according to a predetermined bending radius. After completing a specified number of bending cycles, the resistance at both ends of the film is measured to obtain the relevant data.

Data availability

The data generated in this study is provided in the Source Data file. Source data are provided with this paper.

References

1. Xiao, Y. & Zhao, L.-D. Seeking new, highly effective thermoelectrics. *Science* **367**, 1196 (2020).
2. Jiang, B. et al. High-entropy-stabilized chalcogenides with high thermoelectric performance. *Science* **371**, 830–834 (2021).
3. Chen, W. et al. Nanobinders advance screen-printed flexible thermoelectrics. *Science* **386**, 1265–1271 (2024).
4. Yang, Q. et al. Flexible thermoelectrics based on ductile semiconductors. *Science* **377**, 854–858 (2022).
5. Shi, X.-L. et al. Advancing flexible thermoelectrics for integrated electronics. *Chem. Soc. Rev.* **53**, 9254–9305 (2024).
6. Yu, H. et al. Flexible temperature-pressure dual sensor based on 3D spiral thermoelectric Bi_2Te_3 films. *Nat. Commun.* **15**, 2521 (2024).
7. Du, C. et al. Toward precision recognition of complex hand motions: wearable thermoelectrics by synergistic 2D nanostructure confinement and controlled reduction. *Adv. Funct. Mater.* **32**, 2206083 (2022).
8. Guo, X., Lu, X., Jiang, P. & Bao, X. Touchless thermosensation enabled by flexible infrared photothermoelectric detector for temperature prewarning function of electronic skin. *Adv. Mater.* **36**, 2313911 (2024).
9. Zhang, Q., Deng, K., Wilkens, L., Reith, H. & Nielsch, K. Micro-thermoelectric devices. *Nat. Electron* **5**, 333–347 (2022).
10. Liu, R., Wang, Z. L., Fukuda, K. & Someya, T. Flexible self-charging power sources. *Nat. Rev. Mater.* **7**, 870–886 (2022).
11. Zhai, R.-S. & Zhu, T.-J. Improved thermoelectric properties of zone-melted p-type bismuth-telluride-based alloys for power generation. *Rare Met.* **41**, 1490–1495 (2022).
12. Tian, B.-Z. et al. Low lattice thermal conductivity and enhanced thermoelectric performance of SnTe *via* chemical electroless plating of Ag. *Rare Met.* **41**, 86–95 (2022).
13. Cao, T. et al. Advances in bismuth-telluride-based thermoelectric devices: progress and challenges. *eScience* **3**, 100122 (2023).
14. Shi, X.-L., Zou, J. & Chen, Z.-G. Advanced thermoelectric design: from materials and structures to devices. *Chem. Rev.* **120**, 7399–7515 (2020).

15. Lu, Y. et al. Staggered-layer-boosted flexible Bi_2Te_3 films with high thermoelectric performance. *Nat. Nanotechnol.* **18**, 1281–1288 (2023).
16. Hu, B. et al. Advances in flexible thermoelectric materials and devices fabricated by magnetron sputtering. *Small Sci.* **5**, 2300061 (2025).
17. Wu, H., Shi, X. -l., Duan, J., Liu, Q. & Chen, Z.-G. Advances in Ag_2Se-based thermoelectrics from materials to applications. *Energy Environ. Sci.* **16**, 1870–1906 (2023).
18. Wang, H. et al. Flexible porous Ag_2Se films: from freestanding inorganic films to inorganic-network/organic-skeleton thermoelectric generators. *Adv. Funct. Mater.* **35**, 2413605 (2025).
19. Chen, Y.-X. et al. Deviceization of high-performance and flexible Ag_2Se films for electronic skin and servo rotation angle control. *Nat. Commun.* **15**, 8356 (2024).
20. Franke, L. et al. High power density $Ag_2Se/Sb_{1.5}Bi_{0.5}Te_3$-based fully printed origami thermoelectric module for low-grade thermal energy harvesting. *Adv. Funct. Mater.* **34**, 2403646 (2024).
21. Hu, Q.-X. et al. Carrier separation boosts thermoelectric performance of flexible n-type Ag_2Se-based films. *Adv. Energy Mater.* **14**, 2401890 (2024).
22. Liu, Y. et al. Fully inkjet-printed Ag_2Se flexible thermoelectric devices for sustainable power generation. *Nat. Commun.* **15**, 2141 (2024).
23. Li, Y. et al. Exceptionally high power factor Ag_2Se/Se/polypyrrole composite films for flexible thermoelectric generators. *Adv. Funct. Mater.* **32**, 2106902 (2022).
24. Cao, T. et al. Advancing Ag_2Se thin-film thermoelectrics *via* selenization-driven anisotropy control. *Nat. Commun.* **16**, 1555 (2025).
25. Jiang, C. et al. Ultrahigh performance of n-Type Ag_2Se films for flexible thermoelectric power generators. *ACS Appl. Mater. Interfaces* **12**, 9646–9655 (2020).
26. Liu, Y. et al. Nanoengineering approach toward high power factor Ag_2Se/Se composite films for flexible thermoelectric generators. *ACS Appl. Mater. Interfaces* **15**, 36587–36593 (2023).
27. Gao, Q. et al. High power factor Ag/Ag_2Se composite films for flexible thermoelectric generators. *ACS Appl. Mater. Interfaces* **13**, 14327–14333 (2021).
28. Jiang, C. et al. Ultrahigh performance polyvinylpyrrolidone/Ag_2Se composite thermoelectric film for flexible energy harvesting. *Nano Energy* **80**, 105488 (2021).
29. Lu, Y. et al. Nanoengineering approach toward ultrahigh power factor Ag_2Se/polyvinylpyrrolidone composite film for flexible thermoelectric generator. *Chem. Eng. J.* **485**, 149793 (2024).
30. Lu, Y. et al. Ultrahigh performance PEDOT/Ag_2Se/CuAgSe composite film for wearable thermoelectric power generators. *Mater. Today Phys.* **14**, 100223 (2020).
31. Zhou, H., Zhang, Z., Sun, C., Deng, H. & Fu, Q. Biomimetic approach to facilitate the high filler content in free-standing and flexible thermoelectric polymer composite films based on PVDF and Ag_2Se nanowires. *ACS Appl Mater. Interfaces* **12**, 51506–51516 (2020).
32. Wu H. et al. Sandwich engineering advances ductile thermoelectrics. *Adv. Mater.*, 2503020. https://doi.org/10.1002/adma.202503020 (2025).
33. Lu, Y. et al. Ultrahigh power factor and flexible silver selenide-based composite film for thermoelectric devices. *Energy Environ. Sci.* **13**, 1240–1249 (2020).
34. Wu, M. et al. High Thermoelectric Performance and Ultrahigh Flexibility $Ag_2S_{1-x}Se_x$ film on a Nylon Membrane. *ACS Appl. Mater. Interfaces* **15**, 8415–8423 (2023).
35. Konar, R. et al. Facile and scalable ambient pressure chemical vapor deposition-assisted synthesis of layered silver selenide (β-Ag_2Se) on Ag foil as a possible oxygen reduction catalyst in alkaline medium. *Electrochim. Acta* **370**, 137709 (2021).
36. Zheng, Z.-H. et al. Significantly (00*l*)-textured Ag_2Se thin films with excellent thermoelectric performance for flexible power applications. *J. Mater. Chem. A* **10**, 21603–21610 (2022).
37. Jindal, S., Singh, S., Saini, G. S. S. & Tripathi, S. K. Optimization of thermoelectric power factor of (013)-oriented Ag_2Se films *via* thermal annealing. *Mater. Res. Bull.* **145**, 111525 (2022).
38. Vinodhini, J. et al. Solvent-assisted synthesis of Ag_2Se and Ag_2S nanoparticles on carbon fabric for enhanced thermoelectric performance. *J. Colloid Int. Sci.* **651**, 436–447 (2023).
39. Kongsip, N., Kaewmaraya, T., Kamwanna, T. & Pinitsoontorn, S. Enhancing thermoelectric properties of silver selenide through cold sintering process using aqua regia as a liquid medium. *Materials* **3**, 100136 (2024).
40. Yang, D. et al. Flexible power generators by Ag_2Se thin films with record-high thermoelectric performance. *Nat. Commun.* **15**, 923 (2024).
41. Imasato, K., Kang, S. D. & Snyder, G. J. Exceptional thermoelectric performance in $Mg_3Sb_{0.6}Bi_{1.4}$ for low-grade waste heat recovery. *Energy Environ. Sci.* **12**, 965–971 (2019).
42. Kuo, J. J. et al. Grain boundary dominated charge transport in Mg_3Sb_2-based compounds. *Energy Environ. Sci.* **11**, 429–434 (2018).
43. Feng, B. et al. Ag interstitial inhibition and phonon scattering at the ZnSe nano-precipitates to enhance the thermoelectric performance of Ag_2Se. *ACS Appl. Energy Mater.* **6**, 2804–2811 (2023).
44. Deng, Q. et al. Ordered grain boundary reconstruction induces high-efficiency thermoelectric power generation in SnTe. *Energy Environ. Sci.* **17**, 9467–9478 (2024).
45. Ding, Y. et al. High performance n-type Ag_2Se film on nylon membrane for flexible thermoelectric power generator. *Nat. Commun.* **10**, 841 (2019).
46. Geng, J. et al. High power factor n-type Ag_2Se/SWCNTs hybrid film for flexible thermoelectric generator. *J. Phys. D Appl. Phys.* **54**, 434004 (2021).
47. Hou, S. et al. Encapsulated Ag_2Se-based flexible thermoelectric generator with remarkable performance. *Mater. Today Phys.* **38**, 101276 (2023).
48. Hu, Q.-X. et al. SWCNTs/Ag_2Se film with superior bending resistance and enhanced thermoelectric performance via in situ compositing. *Chem. Eng. J.* **457**, 141024 (2023).
49. Lei, Y. et al. Microstructurally tailored thin β-Ag_2Se films towards commercial flexible thermoelectrics. *Adv. Mater.* **34**, 2104786 (2021).
50. Li, J., Liu, Y., Wang, Z., Chen, L. & Cai, K. Ultra-flexible self-supporting Ag_2Se/nylon composite films for wearable thermoelectric devices. *Compos. Part B-Eng.* **265**, 110946 (2023).
51. Liang, J. et al. Modulation of the morphotropic phase boundary for high-performance ductile thermoelectric materials. *Nat. Commun.* **14**, 8442 (2023).
52. Wang, Z., Liu, Y., Li, J., Huang, C. & Cai, K. High-performance Ag_2Se film by a template method for flexible thermoelectric generator. *Mater. Today Phys.* **36**, 101147 (2023).
53. Lin, S. et al. Revealing the promising near-room-temperature thermoelectric performance in Ag_2Se single crystals. *J. Materiomics* **9**, 754–761 (2023).
54. Liu, Q.-Y. et al. Advances and challenges in inorganic bulk-based flexible thermoelectric devices. *Prog. Mater. Sci.* **150**, 101420 (2024).
55. Mayers, B. T., Liu, K., Sunderland, D. & Xia, Y. Sonochemical synthesis of trigonal selenium nanowires. *Chem. Mater.* **15**, 3852–3858 (2003).
56. Zhang, J., Fu, Q., Xue, Y. & Cui, Z. Controlled synthesis of t-Se nanomaterials with various morphologies *via* a precursor conversion method. *CrystEngComm* **20**, 1220–1231 (2018).

57. Adam, M., Vakifahmetoglu, C., Colombo, P., Wilhelm, M. & Grathwohl, G. Polysiloxane-derived ceramics containing nanowires with catalytically active tips. *J. Am. Ceram. Soc.* **97**, 959–966 (2014).
58. Lei, M., Zhang, Y. B., Fu, X. L., Yang, H. J. & Wang, Y. G. Selective growth of TiO_2 tips on CdSe nanowires. *J. Alloy. Compd.* **513**, 14–17 (2012).
59. Bu, L. et al. Facet and dimensionality control of Pt nanostructures for efficient oxygen reduction and methanol oxidation electrocatalysts. *Nano Res.* **9**, 2811–2821 (2016).
60. Ni, B. & Wang, X. Face the edges: catalytic active sites of nanomaterials. *Adv. Sci.* **2**, 1500085 (2015).
61. Fu, X., Dong, X., Yang, G. & Bai, S. Non-isothermal crystallization kinetics of graphene/PA10T composites. *Heliyon* **8**, e10206 (2022).
62. Perrotta, M. L. et al. Graphene stimulates the nucleation and growth rate of NaCl crystals from hypersaline solution *via* membrane crystallization. *Environ. Sci. Water Res.* **6**, 1723–1736 (2020).
63. Wang, J. et al. Graphene-quantum-dots-induced centimeter-sized growth of monolayer organic crystals for high-performance transistors. *Adv. Mater.* **32**, 2003315 (2020).
64. Suter, J. L. & Coveney, P. V. Principles governing control of aggregation and dispersion of aqueous graphene oxide. *Sci. Rep.* **11**, 22460 (2021).
65. Wang, S. et al. Reduced graphene oxides modified Bi_2Te_3 nanosheets for rapid photo-thermoelectric catalytic therapy of bacteria-infected wounds. *Adv. Funct. Mater.* **33**, 2210098 (2023).
66. Feng, B., Xie, J., Cao, G., Zhu, T. & Zhao, X. Enhanced thermoelectric properties of *p*-type $CoSb_3$/graphene nanocomposite. *J. Mater. Chem. A* **1**, 13111–13119 (2013).
67. Seo, O., Chung, J. & Jo, J. Incomplete oxidation in back channel of GaInZnO thin-film transistor grown by rf sputtering. *Eur. Phys. J. Appl Phys.* **54**, 10302 (2011).
68. Liu, B. et al. Graphene oxide-assisted molecular crystal co-assembly for large-scale freestanding 2D photoresponse heterostructures with synaptic plasticity. *Adv. Mater. Technol.* **9**, 2302017 (2024).
69. Li, D., Ning, X.-A., Li, Y. & Zhang, J. Nanoarchitectured reduced graphene oxide composite C_2N materials as flow electrodes to optimize desalination performance. *Environ. Sci. Nano* **7**, 1980–1989 (2020).
70. Jin, Q. et al. Flexible layer-structured Bi_2Te_3 thermoelectric on a carbon nanotube scaffold. *Nat. Mater.* **18**, 62–68 (2019).
71. Perez-Taborda, J. A., Caballero-Calero, O., Vera-Londono, L., Briones, F. & Martin-Gonzalez, M. High thermoelectric *zT* in n-type silver selenide films at room temperature. *Adv. Energy Mater.* **8**, 1702024 (2018).
72. Zhao, S. et al. Functionally graded graphene reinforced composite structures: a review. *Eng. Struct.* **210**, 110339 (2020).
73. Song, N., Gao, Z. & Li, X. Tailoring nanocomposite interfaces with graphene to achieve high strength and toughness. *Sci. Adv.* **6**, eaba7016 (2020).
74. Chen, D., Li, J., Sun, K. & Fan, J. Graphene-reinforced metal matrix composites: fabrication, properties, and challenges. *Int. J. Adv. Manuf. Technol.* **125**, 2925–2965 (2023).
75. Li, A. et al. High performance magnesium-based plastic semiconductors for flexible thermoelectrics. *Nat. Commun.* **15**, 5108 (2024).
76. Zhao, P. et al. Plasticity in single-crystalline Mg_3Bi_2 thermoelectric material. *Nature* **631**, 777–782 (2024).
77. Deng, T. et al. High thermoelectric power factors in plastic/ductile bulk $SnSe_2$-based crystals. *Adv. Mater.* **36**, 2304219 (2024).
78. Deng, T. et al. Room-temperature exceptional plasticity in defective Bi_2Te_3-based bulk thermoelectric crystals. *Science* **386**, 1112–1117 (2024).
79. Zheng, Z.-H. et al. Harvesting waste heat with flexible Bi_2Te_3 thermoelectric thin film. *Nat. Sustain* **6**, 180–191 (2023).
80. Singkaselit, K., Sakulkalavek, A. & Sakdanuphab, R. Effects of annealing temperature on the structural, mechanical and electrical properties of flexible bismuth telluride thin films prepared by high-pressure RF magnetron sputtering*. *Adv. Nat. Sci: Nanosci. Nanotechnol.* **8**, 035002 (2017).
81. Fan, P. et al. High-performance bismuth telluride thermoelectric thin films fabricated by using the two-step single-source thermal evaporation. *J. Alloy. Compd.* **819**, 153027 (2020).
82. Hu, B. et al. High-performing flexible Mg_3Bi_2 thin-film thermoelectrics. *Adv. Sci.* **11**, 2409788 (2024).
83. Shao, Y. et al. High thermoelectric performance of n-type Mg_3Bi_2 films deposited by magnetron sputtering. *Vacuum* **220**, 112791 (2024).
84. Bhagyashree, P. et al. Synthesis and characterization of polycrystalline SnSe/$SnSe_2$ heterophase thermoelectric thin films *via* chemical spray pyrolysis. *J. Mater. Sci.-Mater. El* **35**, 1895 (2024).
85. Jiang, F. et al. Prefer-oriented Ag_2Se crystal for high-performance thermoelectric cooling. *Adv. Funct. Mater.* **35**, 2415000 (2025).

Acknowledgements

This work was supported by the National Key Research and Development Program of China (2024YFB3813800), Shandong Provincial Natural Science Foundation (ZR2023QE028), China Postdoctoral Science Foundation (2021M703198, 2022M723128), the Dalian National Laboratory for Clean Energy (DNL), CAS, DNL Cooperation Fund, CAS (DNL202021), and the Youth Innovation Promotion Association of the Chinese Academy of Sciences (Y202041). Z.G.C. thanks the financial support from the Australian Research Council, HBIS-UQ Innovation Centre for Sustainable Steel project, and the QUT Capacity Building Professor Program, and acknowledge the National Computational Merit Allocation Scheme (NCMAS 2025), sponsored by National Computational Infrastructure, for providing computational resources and service. This work was enabled by using the Central Analytical Research Facility hosted by the Institute for Future Environments at QUT.

Author contributions

F. D., Z.-G.C. and H. S. supervised the overall experiments. L.Z. designed the related experiments. L.Z., H.D., D.H., and X.W. prepared materials and measured the thermoelectric properties, designed device structures, fabricated devices, and measured the performance. H.S., X.-L.S., H.G., F.D., and Z.-G.C. analyzed the data. W.C. performed the device numerical simulation and M.L. conducted the DFT calculations. H.S., H.G., and X.-L.S. discussed the results. L.Z. wrote the manuscript with the help of all the authors.

Competing interests

The authors declare no competing interests.

Additional information

Supplementary information The online version contains supplementary material available at https://doi.org/10.1038/s41467-025-60284-5.

Correspondence and requests for materials should be addressed to Hongjing Shang, Fazhu Ding or Zhi-Gang Chen.

Peer review information *Nature Communications* thanks KDM Rao, and the other, anonymous, reviewer(s) for their contribution to the peer review of this work. A peer review file is available.

Reprints and permissions information is available at http://www.nature.com/reprints

Publisher's note Springer Nature remains neutral with regard to jurisdictional claims in published maps and institutional affiliations.

Open Access This article is licensed under a Creative Commons Attribution-NonCommercial-NoDerivatives 4.0 International License, which permits any non-commercial use, sharing, distribution and reproduction in any medium or format, as long as you give appropriate credit to the original author(s) and the source, provide a link to the Creative Commons licence, and indicate if you modified the licensed material. You do not have permission under this licence to share adapted material derived from this article or parts of it. The images or other third party material in this article are included in the article's Creative Commons licence, unless indicated otherwise in a credit line to the material. If material is not included in the article's Creative Commons licence and your intended use is not permitted by statutory regulation or exceeds the permitted use, you will need to obtain permission directly from the copyright holder. To view a copy of this licence, visit http://creativecommons.org/licenses/by-nc-nd/4.0/.

© The Author(s) 2025